Research Article | Vol. 8, No. 2 | 1 Feb 2017 | BIOMEDICAL OPTICS EXPRESS 570
Biomedical Optics EXPRESS

Cellular resolution multiplexed FLIM tomography with dual-color Bessel beam

DONGLI XU,[1] WEIBIN ZHOU,[2] AND LEILEI PENG[1,3,*]

[1]*College of Optical Sciences, the University of Arizona, 1630 East University Blvd., Tucson, AZ 85721, USA*
[2]*Department of Pediatrics and Communicable Diseases, University of Michigan, Ann Arbor, Michigan, MI 48109, USA*
[3]*Department of Molecular and Cell Biology, University of Arizona, 1007 E. Lowell Street, Tucson. AZ 85721, USA*
[*]*lpeng@optics.arizona.edu*

Abstract: Fourier multiplexed FLIM (FmFLIM) tomography enables multiplexed 3D lifetime imaging of whole embryos. In our previous FmFLIM system, the spatial resolution was limited to 25 μm because of the trade-off between the spatial resolution and the imaging depth. In order to achieve cellular resolution imaging of thick specimens, we built a tomography system with dual-color Bessel beam. In combination with FmFLIM, the Bessel FmFLIM tomography system can perform parallel 3D lifetime imaging on multiple excitation-emission channels at a cellular resolution of 2.8 μm. The image capability of the Bessel FmFLIM tomography system was demonstrated by 3D lifetime imaging of dual-labeled transgenic zebrafish embryos.

OCIS codes: (110.0110) Imaging systems; (170.2520) Fluorescence microscopy; (170.6280) Spectroscopy, fluorescence and luminescence; (180.6900) Three-dimensional microscopy.

References and links

1. J.-A. Conchello and J. W. Lichtman, "Optical sectioning microscopy," Nat. Methods **2**(12), 920–931 (2005).
2. F. Helmchen and W. Denk, "Deep tissue two-photon microscopy," Nat. Methods **2**(12), 932–940 (2005).
3. J. Sharpe, U. Ahlgren, P. Perry, B. Hill, A. Ross, J. Hecksher-Sørensen, R. Baldock, and D. Davidson, "Optical projection tomography as a tool for 3D microscopy and gene expression studies," Science **296**(5567), 541–545 (2002).
4. J. Sharpe, "Optical Projection Tomography," Annu. Rev. Biomed. Eng. **6**(1), 209–228 (2004).
5. J. R. Walls, J. G. Sled, J. Sharpe, and R. M. Henkelman, "Resolution improvement in emission optical projection tomography," Phys. Med. Biol. **52**(10), 2775–2790 (2007).
6. M. Zhao and L. Peng, "Multiplexed fluorescence lifetime measurements by frequency-sweeping Fourier spectroscopy," Opt. Lett. **35**(17), 2910–2912 (2010).
7. M. Zhao, Y. Li, and L. Peng, "Parallel excitation-emission multiplexed fluorescence lifetime confocal microscopy for live cell imaging," Opt. Express **22**(9), 10221–10232 (2014).
8. R.-A. Lorbeer, M. Heidrich, C. Lorbeer, D. F. Ramírez Ojeda, G. Bicker, H. Meyer, and A. Heisterkamp, "Highly efficient 3D fluorescence microscopy with a scanning laser optical tomograph," Opt. Express **19**(6), 5419–5430 (2011).
9. M. Zhao, X. Wan, Y. Li, W. Zhou, and L. Peng, "Multiplexed 3D FRET imaging in deep tissue of live embryos," Sci. Rep. **5**, 13991 (2015).
10. Z. Ding, H. Ren, Y. Zhao, J. S. Nelson, and Z. Chen, "High-resolution optical coherence tomography over a large depth range with an axicon lens," Opt. Lett. **27**(4), 243–245 (2002).
11. R. A. Leitgeb, M. Villiger, A. H. Bachmann, L. Steinmann, and T. Lasser, "Extended focus depth for Fourier domain optical coherence microscopy," Opt. Lett. **31**(16), 2450–2452 (2006).
12. L. Liu, J. A. Gardecki, S. K. Nadkarni, J. D. Toussaint, Y. Yagi, B. E. Bouma, and G. J. Tearney, "Imaging the subcellular structure of human coronary atherosclerosis using micro-optical coherence tomography," Nat. Med. **17**(8), 1010–1014 (2011).
13. F. O. Fahrbach and A. Rohrbach, "A line scanned light-sheet microscope with phase shaped self-reconstructing beams," Opt. Express **18**(23), 24229–24244 (2010).
14. T. A. Planchon, L. Gao, D. E. Milkie, M. W. Davidson, J. A. Galbraith, C. G. Galbraith, and E. Betzig, "Rapid three-dimensional isotropic imaging of living cells using Bessel beam plane illumination," Nat. Methods **8**(5), 417–423 (2011).

#275798 http://dx.doi.org/10.1364/BOE.8.000570
Journal © 2017 Received 14 Sep 2016; revised 19 Dec 2016; accepted 20 Dec 2016; published 4 Jan 2017

Biomedical Optics EXPRESS

15. M. Zhao, H. Zhang, Y. Li, A. Ashok, R. Liang, W. Zhou, and L. Peng, "Cellular imaging of deep organ using two-photon Bessel light-sheet nonlinear structured illumination microscopy," Biomed. Opt. Express **5**(5), 1296–1308 (2014).
16. F. O. Fahrbach, P. Simon, and A. Rohrbach, "Microscopy with self-reconstructing beams," Nat. Photonics **4**(11), 780–785 (2010).
17. F. O. Fahrbach and A. Rohrbach, "Propagation stability of self-reconstructing Bessel beams enables contrast-enhanced imaging in thick media," Nat. Commun. **3**, 632 (2012).
18. J. Leach, G. M. Gibson, M. J. Padgett, E. Esposito, G. McConnell, A. J. Wright, and J. M. Girkin, "Generation of achromatic Bessel beams using a compensated spatial light modulator," Opt. Express **14**(12), 5581–5587 (2006).
19. M. Zhao, Y. Li, and L. Peng, "FPGA-based multi-channel fluorescence lifetime analysis of Fourier multiplexed frequency-sweeping lifetime imaging," Opt. Express **22**(19), 23073–23085 (2014).

1. Introduction

Three-dimensional optical microscopic methods allow the visualization of structural and functional information inside thick tissue and embryos. They have become powerful tools for biologist to study live specimen noninvasively. Still, two major challenges remain in the field of 3D optical imaging of biological samples: first, penetrating thick specimens while maintaining cellular-level resolution and high sensitivity, and second, obtaining more functional information while keeping the same imaging speed.

The penetration depth of a microscopy method is limited by tissue scattering. Conventional optical microscopy assumes light travels along a ballistic path in a biological specimen. In reality, light scattering exists both in the illumination/excitation and the emission path, and the sensitivity and resolution of conventional optical microscopy methods degrade in deep tissue. For example, commercial microscopes based on point-scanning imaging, such as confocal and multi-photon imaging, require a tightly focused excitation beam, which spreads out in deep tissue due to scattering, resulting in resolution degradation. Confocal microscopy uses a pinhole to reject diffused fluorescence signal [1], leading to low detection efficiency in deep tissue. Multi-photon microscopy, while having better tissue penetration due to the use of long wavelength light [2], still needs to battle with the loss of excitation power and maintain a delicate balance between fluorescence emission strength, imaging speed and photo-damage. The same penetration limit also applies to more recent optical imaging methods specialized in deep tissue imaging. For example, Optical projection tomography (OPT), which uses a camera to capture projection images of a specimen, has the ability to image 3D morphology of specimens by light absorption or fluorescence [3], but when imaging large specimens, the resolution of camera-based OPT is significantly degraded [4]. In light sheet imaging, images from the center of a specimen are often significantly weakened and blurred [5]. Both camera-based OPT and light sheet microscopy suffer from light scattering degradation in the excitation and detection path. Scanning laser optical tomography (SLOT) [8], the raster-scanning optical tomography method, however, only suffers from light scattering in the excitation path. Because the emission signal of SLOT is collected pixel-by-pixel through condensing optics rather than imaging optics, scattered emission can be effectively collected and spatially registered in an SLOT projection image. SLOT in theory has a longer penetration depth than camera-based OPT and light sheet imaging.

Functional information from a specimen can be obtained by combining structural image detection with spectroscopic measurements. Recently, we presented the combination of Fourier multiplexed fluorescence lifetime imaging (FmFLIM) [6, 7] and SLOT. FmFLIM-SLOT performed non-invasive quantitative lifetime imaging of multiple FRET sensors in deep tissue, which allowed multiplexed 3D functional image analysis of live zebrafish embryos [9]. However, at present, the resolution of the SLOT was limited at the macroscopic level, which was set by the cross section of the Gaussian scanning beam [8,9]. Although a tightly focused Gaussian beam could potentially support SLOT at the cellular resolution, the rapid divergence of a Gaussian beam would prohibit tomographic imaging over a large

Biomedical Optics EXPRESS

specimen. In our previous FLIM-SLOT study, in order to image the entire zebrafish embryo, which is over 300 μm in its thickest part, a trade-off between spatial resolution and field of view (FOV) was made, and the experimental resolution was set at 25 μm.

Here we report the use of a dual-color Bessel beam in the FmFLIM-SLOT to achieve cellular resolution functional imaging with an extended field of view. Results will show the Bessel FmFLIM-SLOT system achieves a spatial resolution of 2.8 μm in a 705-μm-wide FOV. The resolution of the new system is 1/10 of the resolution of the previous Gaussian FmFLIM-SLOT system. Meanwhile, the Bessel FmFLIM-SLOT system is still capable of performing multiplexed 3D lifetime imaging of live embryos, and can be used for multiplexed FLIM-FRET imaging *in vivo*.

2. Bessel multiplexed FLIM tomography

The Bessel beam is well-known for its 'non-diffraction' pencil shape focus. Compared to a Gaussian beam, the Bessel beam has an extended focal depth with narrow central peak. It has been used in optical coherence tomography [10–12] and light sheet microscopy [13–15] to improve resolution over an extended imaging depth. Similarly, replacing the Gaussian beam with a Bessel beam in SLOT will improve the resolution without sacrificing the image depth. The self-reconstructing nature of a Bessel beam can also reduce scattering artifacts, and increase penetration depth of excitation photons in inhomogeneous media [16, 17].

The FmFLIM-SLOT system, as demonstrated previously, has the unique ability of parallel excitation-multiplexing (Fig. 1(A)). In the system, a multi-wavelength laser beam is modulated by a fast-scanning Michelson interferometer, which generates intensity modulations in the laser (Fig. 1(B)). Each laser line has its unique modulation frequency, which provides the ability of simultaneous lifetime measurements on multiple excitation channels through the principles of Fourier (frequency) multiplexing. The FmFLIM-SLOT system then uses the modulated multi-wavelength laser beam to scan across the sample and performs tomography imaging. In order to introduce Bessel beam scanning in FmFLIM-SLOT while keeping the benefit of parallel detections on multiple excitation wavelengths, Gaussian beams from multiple laser lines need to be reshaped into Bessel beams co-propagating along the same propagation axis and with the same beam profile, so that images of all laser lines are precisely co-registered and have the same resolution. Such an achromatic Bessel beam cannot be produced with an axicon lens [18]. In our system, a SLM(Spatial light modulator) based method was used to generate the achromatic Bessel beam (Fig. 1(C)) [18].

2.1 Optical setup

Figure 1(A) shows the schematic of the FmFLIM Bessel tomography system. Excitation laser lines (488 nm and 561 nm) are merged and coupled into a single mode fiber. The output from the fiber is collimated, and directed into a Michelson interferometer with a spinning polygon mirror (Lincoln Laser), which is the same as previously reported (Fig. 1(B)). The polygon mirror has 48 facets mirror which scans at a speed of 55,000 rpm (23 μs per facet). It produces a wavelength dependent frequency sweep, whose frequency $f = v/\lambda$ is unique for each laser line (v is the instantaneous delay-scan speed, which changes linearly from approximately –94 m/s to 94 m/s).

The modulated laser output from the interferometer is split into two parts. The weaker part of the output is further split into two laser lines by a dichroic mirror, and sent to two high-speed photodetectors to record interference modulations of two excitation lasers respectively. The majority of the output beam is expanded and directed to an SLM (Hamamatsu, X10468-01, 800 × 600, 20 μm pitch) to create the Bessel beam. The phase change of an SLM is wavelength dependent, which makes an SLM an inherently dispersive component. To achieve identical beam shaping at multiple wavelengths, dispersion compensation is needed. Jonathan *et al.* [18] had demonstrated a SLM-based dispersion compensation method for generating achromatic Bessel beams. We follow their method (Fig. 1(C)) of adding a grating pattern in

Biomedical Optics EXPRESS

additional to the axicon phase pattern on the SLM. An iris is used to select the first-order diffracted component at the Fourier plane. The linear angle dispersion in the multi-wavelength beam, which is caused by the grating, is compensated by a 4° BK7 prism placed in the image plane.

The frequency modulated two-color Bessel beam is directed to a SLOT imaging system. After passing through an x-y galvo mirror scanner, a series of 4f relay lenses and the final illumination objective (M plan Apo 20x, Mitutoyo), the Bessel beam is de-magnified by 80x and projected onto the sample. The embryo is mounted in a transparent FEP tube (Cole Parmer, 06406-60, 1/32 inch ID), whose rotation is controlled by a motorized rotational stage (PRM1Z8, Thorlabs). The Bessel beam scans across the sample and excites fluorophores along its path. Fluorescent emission is collected from the side by a f = 30 mm condenser lens, separated into two emission spectral bands by a dichroic mirror and detected by two PMT detectors (H7422, Hamamatsu).

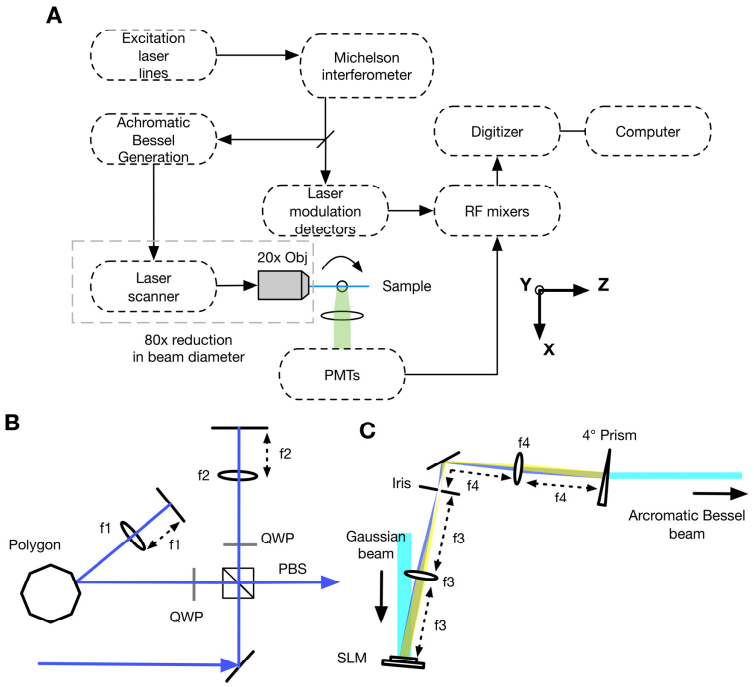

Fig. 1. Schematics of Bessel FmFLIM-SLOT tomography. (A) Schematic of key optical and electronic components of the Bessel FmFLIM-SLOT system. (B) Detailed schematic of the Michelson interferometer, which produces wavelength-dependent frequency sweeping interferometric modulation for all laser lines. f1 = 50 mm, f2 = 50 mm (C) Optical schematic of two-color Bessel beam generation. The modulated Gaussian beam from the Michelson interferometer is expanded and directed to the SLM. An Iris is placed at the Fourier plane of the SLM to select the first order diffracted beams. A 4° prism at the image plane of the SLM is used to compensate the dispersion. f3 = 400 mm, f4 = 250 mm. QWP, quarter-wave plates; PBS, polarizing beamsplitter; SLM, spatial light modulator.

2.2 Characteristics of dual-color Bessel beam

Traditionally, a Bessel beam is generated by passing a circular beam through an axicon lens or a SLM with a wrapped axicon phase pattern. The characteristics of the resulting Bessel beam are decided by a combination of the incident beam size (or the SLM size) and the base angle of the axicon, which is tunable in an SLM. In our setup, the $1/e^2$ radius of the incident beam was $a_0 = 5\ mm$, and a phase pattern equivalent to an axicon base angle $\theta = 0.0015\ rad$ was used to generate the original Bessel beam. Assuming the incident beam is a plane wave,

Biomedical Optics EXPRESS

the resulting Bessel beam was estimated to be $l = a_0/\theta = 3.3\ m$ in length, and its center lobe width should be $r = 0.61\lambda/\theta = 199\ \mu m$ at laser wavelength $\lambda = 488\ nm$. After 80x de-magnification, the Bessel beam at the sample should be 2.5 μm in the center lobe width and 500 μm in the maximum length.

The key to multi-color Bessel beam generation with an SLM is adding a diffractive grating phase pattern on top of the axicon pattern on the SLM, and later using a prism to compensate the linear angle dispersion in the first-order diffracted beam. Figure 2(A) shows Bessel beam profiles of individual wavelengths captured by a beam profiler at 450mm after the prism. The beam profile of each individual wavelength, shown in Fig. 2(B), matches with the ideal Bessel function within the experimental precision. Beams of all wavelengths have a central lobe diameter of 169 μm (zero to zero), which matches the theoretical estimation reasonably well. Because the single-element BK7 prism we used has a non-linear dispersive curve, full dispersion compensation can only be achieved at two wavelengths. Changing the grating line density will allow forming dual-wavelength Bessel in any wavelength combination. In this study, by fine-tuning the line density of the grating pattern, a two-color Bessel beam at 488 and 561 nm was produced, but 405 and 640 nm beams exhibit residue dispersion, which caused beam centers to move away from the 488-561 beam (Fig. 2(C)). A multi-element achromatic prism with a linear dispersion could be used in the future to generate a white achromatic Bessel beam.

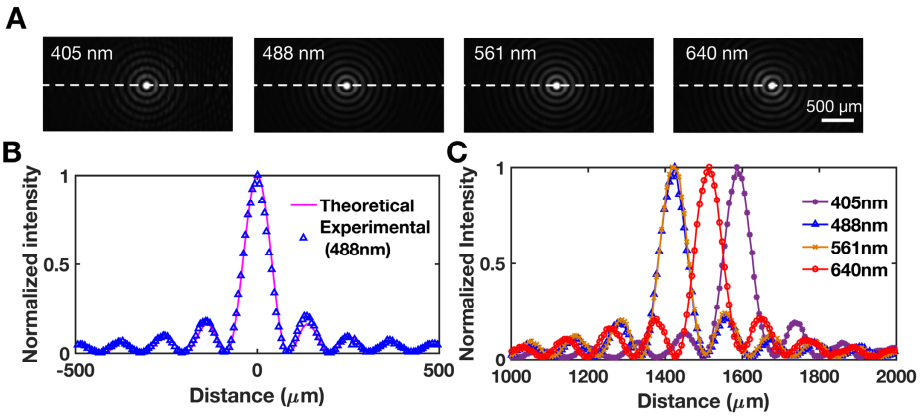

Fig. 2. Cross sectional images of Bessel beams taken after the dispersion compensation from a BK7 prism. (A) Beam profiles from different laser lines (405nm, 488nm, 561nm and 640nm), images are captured by a beam profiler (Thorlabs) at 450mm away from the prism. (B) Theoretical and experimental 488 nm Bessel beam intensity cross-sections taken at the dashed line in A. The diameter of the central lobe is 169 μm (zero to zero) (C) Overlaid cross-sections of all wavelengths, showing the overlap of 488 nm and 561 nm Bessel beams and dispersion residues in 405 nm and 640 nm beams.

After demagnification through a series of delay lens and objective, the achromatic Bessel beam reaches the sample. Its actual length was measured to be about 300 μm in FWHM and its full length was about 500 μm (Fig. 3(A) and Fig. 3(B)). The Bessel FmFLIM-SLOT system can therefore perform 3D imaging over at least 300 μm thick specimen with an isotropic resolution. To experimentally test the imaging resolution over the entire imaging FOV, we took the scattering image of a FEP tube (Cole Parmer, 06406-60, 1/32 inch ID) by removing the emission filter. To stay as close as possible to the situation of live embryo imaging, the tube was filled with 1% low melting point agarose (Sigma), which was used to embed live embryos in later experiments. A thin water gap formed between the agarose and the FEP tube after gelling. In the cross-section view of the 3D reconstructed tube image, weak reflections from the FEP-water interface (outside circle) and water-agar interface (inside circle) were resolved over the entire circular section of the tube cavity, whose diameter was

Biomedical Optics EXPRESS

measured to be 705 μm (Fig. 3(C)). The double-layer circular structure was observed without tomographic reconstruction artifact. Line widths of two interfaces were used to estimate the FWHM of the system's line response function, *i.e.* the resolution. Figure 3(D) plots the line profile across two interfaces, averaged along the entire circle of the tube wall, which show FWHM widths of two interfaces are at 2.8 μm and 2.6 μm respectively. The double-layer circular structure is located at the edge of the FOV, where the tomography image resolution is degraded by the excitation beam divergence. Thus we estimated that the spatial resolution of Bessel-SLOT is 2.8 μm or better within the entire FOV. The experimental resolution estimation (2.8 μm) matches with the theoretical beam size estimation (2.5 μm) within a reasonable error. The side view of the Bessel beam (Fig. 3(A)) also shows slight asymmetry, which was caused by aberrations in the objective lens and slight index mismatching between FEP, water and agarose. Aberrations increase as the Bessel beam scans to the edge of the projection FOV. Thus, the size of the projection image is limited to about 900 μm.

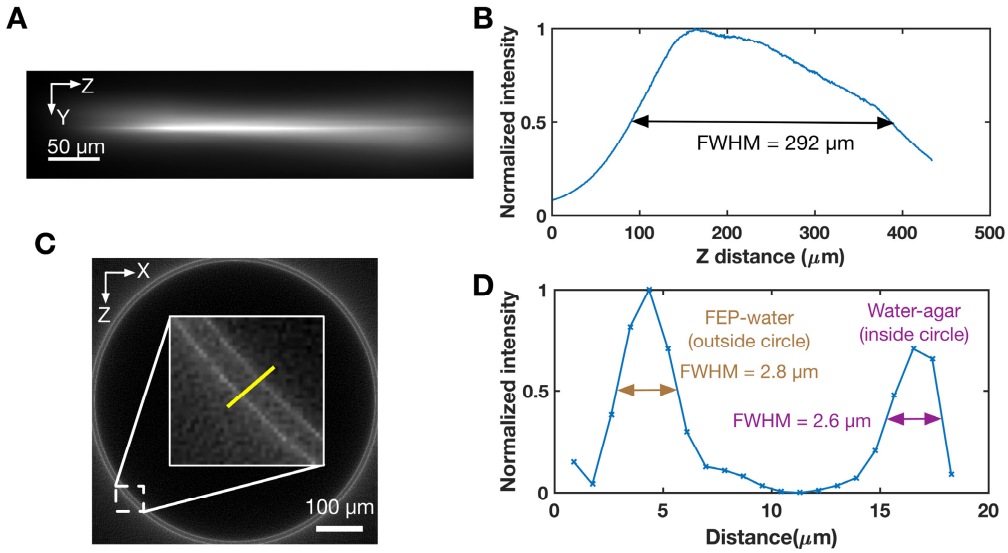

Fig. 3. Characterization of the FOV and resolution. (A) Side projection image of a Bessel beam propagating in a sample tube filled with fluorescent dye. Image is acquired by an EMCCD through a 40x objective (0.8 NA, Olympus) and an 85 mm tube lens. (B) Peak intensity curve along the propagation axis, showing the Bessel beam has a FWHM length of 292 μm. (C) Reconstructed cross-section image of the internal cavity of a FEP tube. (D) Intensity profile across the FEP-water interface (outside circle in C) and water-agar interface (inside circle in C). The profile was calculated by interpolating the image in C along a line (yellow line in C) normal to two interfaces, and averaging all lines around the circular interface. The interpolation step size is 0.9 μm.

2.3 FmFLIM-SLOT data processing

In the same way as our pervious low-resolution FmFLIM-SLOT study, raw data from the Bessel FmFLIM-SLOT underwent 3D image reconstruction followed by multi-channel lifetime analysis. The data processing was discussed in detail previously [9]. In short, the fluorescence emission is split into multiple emission channels through a cascade of dichroic mirrors. Each emission channel is detected by a PMT. The PMT signal is amplified and down mixed with a reference excitation laser modulation signal. The resulting signal contains the amplitude and frequency response phase information about the fluorescence emission for each emission-excitation channel [19]. In FmFLIM-SLOT, signals from multiple excitation-emission channels are digitalized and stored simultaneously during a projection scan, producing a 2D projection image of hyperspectral fluorescence frequency domain data $S(x, z, \theta_i; \omega, \lambda_x, \lambda_m)$, where x, z are the coordinates of projection images, θ_i is the projection angle of

Biomedical Optics EXPRESS

each projection, ω is the sweeping modulation frequency of excitation beam, and $\lambda_{x,m}$ are excitation-emission wavelengths. During data processing, a hyper-spectral 3D volume $S'(x, y, z; \omega, \lambda_x, \lambda_m)$ is first reconstructed from the projection data through the inverse Radon transform. Then the frequency response S' is analyzed by iterative least square fitting with single-exponential decay model [7], which generates the multi-channel 3D fluorescence lifetime image $\tau(x, y, z; \lambda_x, \lambda_m)$ and intensity image $I(x, y, z; \lambda_x, \lambda_m)$.

3. Multiplexed 3D FLIM of live zebrafish embryo

To demonstrate Bessel FmFLIM-SLOT's capability in live imaging, *Tg (kdrl:GFP; fli1a:Gal4; UAS:nfsB-mCherry)* zebrafish embryos were mounted in FEP tubes with embryo medium containing 200 μg/mL tricaine (anesthetic drug) and 1% low melting point agarose gel (Sigma). The triple transgenic embryo expresses GFP in vascular endothelial and lymphatic cells and mCherry in vascular endothelial cells.

A dual-color Bessel beam of 488 and 561 nm was used to scan embryos. Emission was split into green (457 ± 20 nm) and red (593 ± 20 nm). Two excitation-emission channels: 488-green and 561-red were recorded simultaneously to detect GFP and mCherry respectively. Excitation powers were 940 μW (488 nm) and 660 μW (561 nm) at the pupil of the objective lens respectively. The embryo was rotated at 2° angle intervals between each projection. A total of 180 frames 360 × 512 pixels projection images with 1.8 μm pixel pitch were acquired. It took 22 minutes to acquire the whole data set, of which approximately 14 minutes were spent on projection image scanning, and 8 minutes were spent on rotating the embryo.

Figure 4 presents a set of reconstructed 3D image taken from an embryo at 40 hpf (hours post fertilization). Fly through and 3D rendered views of the entire image set are available in Supplementary Visualization 1, Visualization 2, and Visualization 3. In intensity projections and cross-sections, fine structural detail can be seen in vasculature labeled by GFP and mCherry. The expression patterns of GFP and mCherry were not identical because expressions of these two FPs were driven by two different promoters (*kdrl* for GFP and *fli1a* for mCherry). Lifetime images of 488-green and 561-red channels show lifetimes of GFP and mCherry at 2.4 ns and 1.5 ns respectively. In a zoomed view of a reconstructed cross section (Fig. 4(D), 488-green channel), two vascular walls are clearly discerned with a separation of 3.5 μm, indicating that the spatial resolution of Bessel FmFLIM tomography is better than 3.5 μm in a live embryo (Fig. 4(E)).

In Bessel FmFLIM-SLOT, a large fraction of energy propagates in side bands of the Bessel beam and generates a constant fluorescence background in the raw projection image (Fig. 5(C), red line). The background is removed in the reconstructed tomographic 3D image (Fig. 5(C), blue line), because in the inverse Radon transform reconstruction, which is given by

$$u(x,y)=\int P(\theta',k)\exp\left[2\pi ik\left(x\cos\theta+y\sin\theta\right)\right]k\,dkd\theta, \qquad (1)$$

a constant background (spatial frequency $k = 0$) in the projection image $P(\theta, k)$ does not contribute to the result after being multiplied by the inverse filter k.

The background, however, does add unwanted bleaching to samples and contributes additional shot noise to the reconstructed image. Both bleaching and additional shot noise affect the SNR of the results. Because side bands are stronger in narrower and longer Bessel beams, a trade-off between the depth of view and the SNR needs to be made in Bessel SLOT. In this work, the 2.5 μm resolution and a 300 um depth of view were chosen for imaging live zebrafish embryos. In future applications, the resolution and the depth of view may be adjusted by changing the axicon phase pattern on the SLM.

Biomedical Optics EXPRESS

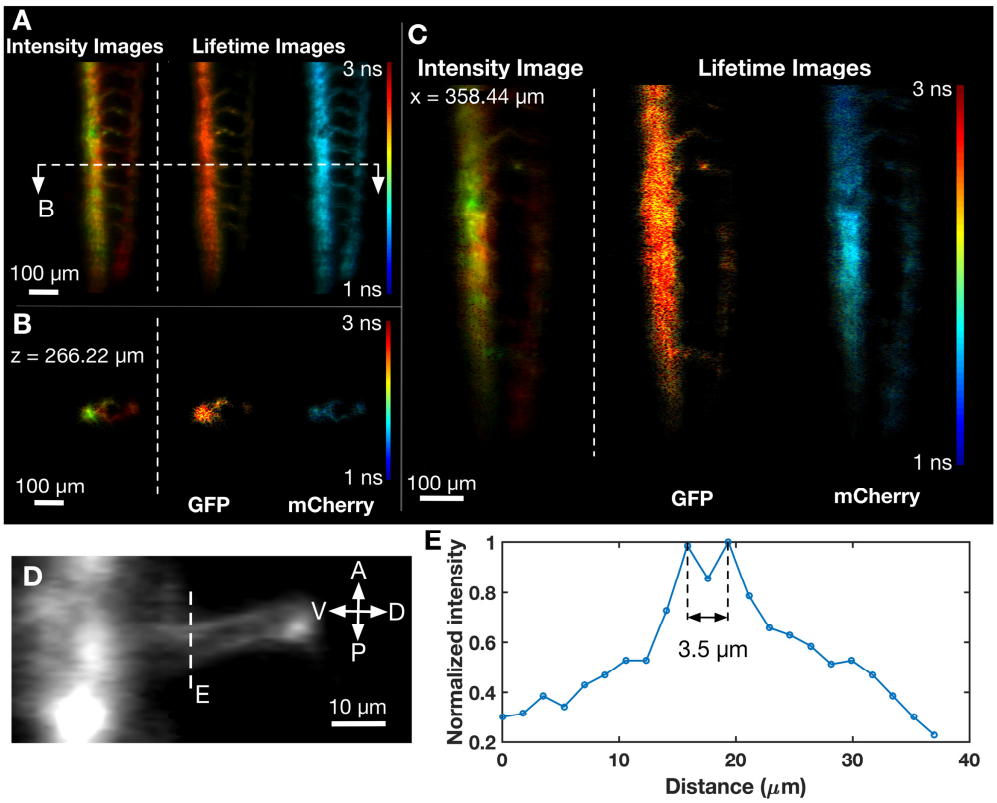

Fig. 4. 3D two-channel lifetime images of the tail of a zebrafish embryo at 40 hpf.

(A) *Left:* Maximum intensity projection 3D tomographic image of GFP (in green) and mCherry (in red), showing GFP and mCherry in vasculature.

Middle: Intensity weighted lifetime maximum projection image of 488-green channel, showing GFP has an average lifetime of 2.4 ns. Lifetime is encoded in false color according to the look-up-table on the right.

Right: Intensity weighted lifetime maximum projection image of 561-red channel, showing mCherry has an average lifetime of 1.5 ns (see Visualization 1).

(B) *Left:* Cross-section intensity image of GFP (in green) and mCherry (in red)

Middle & Right: Lifetime section images of 488-green and 561-red channels, showing GFP and mCherry lifetimes (see Visualization 2).

(C) *Left:* Lateral cross-section intensity image of GFP (in green) and mCherry (in red)

Middle & Right: Lifetime section images of 488-green and 561-red channels, showing GFP and mCherry lifetimes (see Visualization 3).

(D) Zoomed view of a 488-green intensity cross section, showing fine vascular structures.

(E) Normalized intensity profile of the fine vascular structure marked in (D) Two vascular walls were seen separated by 3.5 µm in the reconstructed image.

Biomedical Optics EXPRESS

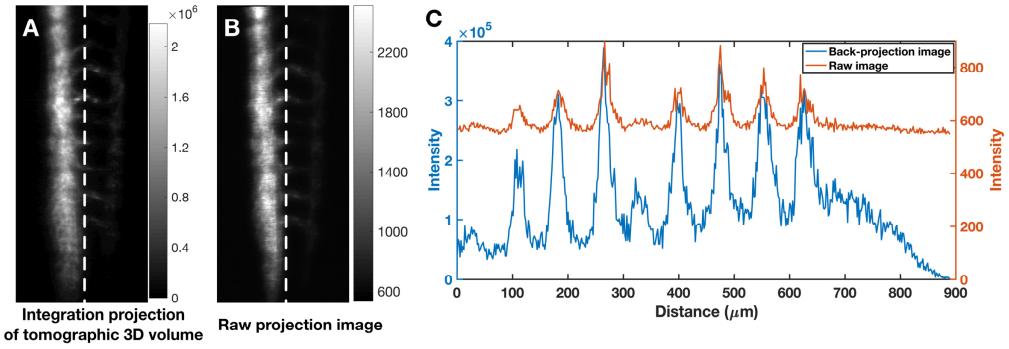

Fig. 5. Background in raw projection images due to Bessel side bands and its removal in the tomography reconstruction (A) Intensity projection image of a zebrafish embryo tail, calculated by integrating the 3D reconstructed image. (B) Raw projection image at the same projection angle of A. (C) Intensity profiles along the dashed lines marked in A and B, showing a uniform background in the raw projection image due to Bessel sidebands (orange line), which was removed in the tomographic 3D image (blue line) after the inverse Radon transform.

4. Summary

By replacing the Gaussian scan beam with a multi-color Bessel beam, the spatial resolution of FmFLIM-SLOT was boosted from 25 μm [9] to 2.8 μm, whereas its depth of view was maintained at more than 300 μm. The 2.8 um resolution is significant for revealing fine cellular structure in live specimen. The system was applied to live zebrafish embryo imaging. Results demonstrated that the sensitivity of the system is sufficient for live imaging of fine structures labeled by genetically expressed fluorescence markers and the experimental resolution reaches the theoretical prediction. Low-resolution FmFLIM-SLOT had been previously used for dual FRET sensor imaging, which allowed dual functional image readout from live embryos during different stages of development. With an improved resolution, Bessel FmFLIM-SLOT will be able to perform similar *in vivo* multiplexed functional imaging study with more spatial information, and provide information about complex spatial-temporal biochemical events during development and disease progression.

Funding

This work is support by National Institutes of Health (NIH) grants L. P. (R00EB008737 and R01EB015481). W.Z. was supported by grants from NIH (R00DK091405), American Society of Nephrology (Carl W. Gottschalk Research Scholar Grant) and National Kidney Foundation.